PtCo/C catalysts with narrow particle size distribution improve high current density operation in PEM fuel cells

Philipp A. Heizmann[1,2,=], Hien Nguyen[1,3,=], Miriam von Holst[1,3], Andreas Fischbach[1], Mitja Kostelec[4], Francisco Javier Gonzalez Lopez[4,5], Marjan Bele[4], Luka Pavko[4], Tina Đukić[4], Martin Šala[6], Francisco Ruiz-Zepeda[4], Carolin Klose[1,3], Matija Gatalo[4,5], Nejc Hodnik[4], Severin Vierrath[1,2,3] and Matthias Breitwieser[1,3,z]

1. Electrochemical Energy Systems, IMTEK - Department of Microsystems Engineering, University of Freiburg, Georges-Koehler-Allee 103, 79110 Freiburg, Germany
2. University of Freiburg, Institute and FIT – Freiburg Center for Interactive Materials and Bioinspired Technologies, Georges-Köhler-Allee 105, 79110 Freiburg, Germany
3. Hahn-Schickard, Georges-Koehler-Allee 103, 79110 Freiburg, Germany
4. Department of Materials Chemistry, National Institute of Chemistry, Hajdrihova ulica 19, 1000 Ljubljana, Slovenia
5. ReCatalyst d.o.o., Hajdrihova ulica 19, Ljubljana, 1000, Slovenia
6. Department of Analytical Chemistry, National Institute of Chemistry, Hajdrihova ulica 19, 1000 Ljubljana, Slovenia

= Equal contribution

z Corresponding author. E-Mail: matthias.breitwieser@hahn-schickard.de

Abstract:

The design of catalysts with stable and finely dispersed platinum on the carbon support is key in controlling the performance of fuel cells. In the present work, an intermetallic PtCo/C catalyst with a narrow particle size distribution synthesized via double-passivation galvanic displacement is demonstrated. The catalyst exhibits an improved high-current-density performance in single-cell low-temperature fuel cell tests. TEM and XRD confirm a significantly narrowed particle size distribution for the catalyst particles in contrast to commercial benchmark catalysts (Umicore PtCo/C 30 and 50 wt%). Only about 10 % of the mass fraction of PtCo particles show a diameter larger than 8 nm, whereas up to > 35 % for the reference systems. This directly results in a considerable increase in electrochemically active surface area (96 $m^2\ g^{-1}$ vs. < 70 $m^2\ g^{-1}$). In addition, a higher fraction of these finely distributed PtCo nanoparticles are anchored on the carbon surface compared to the industrial benchmarks where nanoparticles are located inside the carbon pores. Single-cell tests confirm this finding by a significantly improved performance, especially at high current densities (~ 1 W cm^{-2} at 0.55 V under H_2/air, 50 % RH, 250 kPa_{abs}) and even with lower Pt loading (0.25 $mg_{Pt}\ cm^{-2}$) compared to the commercial reference (< 0.9 W cm^{-2} at the same potential and the given conditions) with a higher Pt loading (0.4 $mg_{Pt}\ cm^{-2}$). Lastly, reducing the cathode catalyst loading from 0.4 to 0.25 mg cm^{-2} resulted in a power density drop at application-relevant 0.7 V of only 4 % for the novel catalyst, compared to the 10 % and 20 % for the Umicore reference catalysts with 30 wt% and 50 wt% PtCo on carbon.

Keywords: Galvanic displacement, PtCo/C, Pt-alloy, fuel cells, high current density operation

1 Introduction

On the way to developing and implementing sustainable clean energy technologies to combat climate change and pollution, proton exchange membrane fuel cells (PEMFCs) present themselves as a promising technology for power source applications in the automobile and energy industries due to their high power density, low operating temperature and fast refueling times.[1] A major barrier to large-scale commercialization is the high cost of PEMFCs, with the common platinum-based catalyst accounting for a substantial portion of the price. The R&D division of Toyota Motor Corporation, manufacturer of one of the first commercially available fuel cell vehicles "Mirai", emphasized the importance of reducing the amount of platinum in the catalyst while maintaining or improving the specific activity and platinum efficiency significantly.[2] At high production volume (500k systems/annually), the platinum-based catalyst represents > 40 % of the total system costs, which will not benefit from the economies of scale.[3–5] Thus, while economies of scale will be a crucial cost reduction driver, it is also critical to reduce the required amount of noble metals in the PEMFC.

Numerous studies showed that Pt*M*/C alloy catalysts (*M* e.g. Co, Ni, Cu, Fe) exhibit an increased activity for the oxygen reduction reaction (ORR) and thus lead to a remarkable performance improvement of the corresponding membrane electrode assembly (MEA) in PEMFCs compared to pure Pt/C based systems.[6–11] Advantageously, the dilution of the particle core with these 3*d* transition metals simultaneously leads to a reduction in the total amount of noble metal.[12] However, the use of these alloying transition metals also comes with two major disadvantages: the higher complexity of the overall catalyst, e.g. regarding the more difficult synthetic access, and the intrinsic thermodynamic instability of the alloy catalysts under acidic

conditions.[13] One approach to the latter problem is to selectively deplete the transition metal concentration at the particle surface to practically prevent the dissolution while preserving the positive influences of alloy formation (ligand and crystal strain effects) as much as possible. For example, PtCo nanoparticles with Pt-rich shell of ~3 atomic layers still exhibits significantly improved ORR activity.[14, 15] The process of Pt-rich shell formation (in other words, depletion of *M* from the Pt*M* shell) can be accomplished by electrodissolution or by washing in acidified solutions.[16–18]

In addition to fundamental research focusing on improving the performance and stability of the catalysts, studies on optimization and scalable synthesis routes are as important.[18–23] In the last years, some research has tackled this topic. For instance, Gatalo *et al.* reported a novel double passivation galvanic displacement method for Pt-alloy catalysts with high reproducibility and great flexibility allowing a highly targeted catalyst design, where the chemical composition and loading of the alloy on the carbon support can be tuned very precisely.[24] This approach can potentially be applied to a wide range of sacrificial metals *M* and on a variety of carbon supports while allowing the production of the resulting catalyst on a multigram scale.[25] In these studies, the reported synthesized catalysts showed promising electrochemical improvements in both rotating-disk electrode (RDE) and gas-diffusion electrode (GDE) tests compared to commercially available catalysts, including higher specific activities (SA), mass activities (MA) and electrochemical surface areas (ECSA).

In the present study, we take advantage of the promising catalytic activity for the ORR and the great ECSA of the Pt-alloy catalyst based on double passivation galvanic displacement.[24–26] We confirm the significantly narrower particle size distribution of the novel PtCo/C catalysts compared to commercial PtCo/C catalysts via transmission scanning electron microscopy (TEM) image analysis and X-ray powder diffraction (XRD). In addition, the effect of the significantly narrowed particle size distribution on the performance is demonstrated with thin-film rotating disk electrodes (TF-RDEs) and in 4 cm² single-cell MEAs under different industry-relevant conditions. Besides showcasing the exceptionally high performance of the new catalyst in comparison to the PtCo/C benchmarks from Umicore we also propose a link between the higher ECSA and the observed higher single-cell performance, especially at high current density and reduced loading.

2 Experimental

2.1 Catalyst synthesis

The synthesis of the new experimental PtCo/C catalyst (hereafter referred to as ReCatalyst) was based on the previous works and can be conceptualized into four main steps:[24–26] (I) Preparation of the Co/C composite (cobalt nanoparticles on commercial carbon black, Ketjenblack EC300J) via the pulse combustion method; (II) Deposition of platinum nanoparticles via the double passivation with galvanic displacement method using part of the cobalt from the Co/C composite as the sacrificial base metal to obtain a Pt+Co/C composite; III) Thermal annealing of the as-synthesized Pt+Co/C composite to obtain a PtCo alloy with the desired intermetallic crystal phase; IV) Dealloying of the PtCo/C catalyst as described in literature.[27, 28]

2.2 Characterization

2.2.1 Inductively coupled plasma optical emission spectrometry (ICP-OES)

All reagents used were of analytical grade or better. For sample dilution and preparation of standards, ultrapure water (18.2 MΩ cm^{-1} , Milli-Q, Millipore) and ultrapure acids (HNO_3 and HCl, Merck-Suprapur) were used. Standards were prepared inhouse by dilution of certified, traceable, inductively coupled plasma (ICP)-grade single-element standards (Merck CertiPUR). A Varian 715-ES ICP optical emission spectrometer was used. Before ICP-OES analysis, each catalyst powder was weighted (approximately 10 mg) and digested using a microwave-assisted digestion system (Milestone, Ethos 1) in a solution of 6 mL HCl (conc.) and 2 mL HNO_3 (conc.). Samples were then filtered, and the filter paper was again submitted to the same digestion protocol. These two times digested samples were cooled to room temperature and then diluted with 2 % v/v HNO_3 until the concentration was within the desired concentration range.

2.2.2 X-ray Powder Diffraction (XRD)

All X-ray diffractograms were acquired on a X'Pert PRO diffractometer (Malvern Panalytical) with Cu Kα radiation (λ = 1.541874 Å). The powder samples were prepared on a zero-background Si holder and measured in the 2θ range from 10° to 60° with a step size of 0.039° per 300 s by using a fully opened Pixcel detector.

2.2.3 Transmission scanning electron microscopy (S/TEM)

TEM micrographs were recorded on a Talos F200X (S)TEM (ThermoFisher, high-brightness X-FEG emitter) at 200 kV acceleration voltage with a Ceta 16 Megapixel CMOS Camera. Samples were dispersed in isopropyl alcohol, briefly sonicated (Bandelin Sonorex super RK 100 H) and loaded onto copper TEM grids (carbon film, 3-4 nm nominal thickness, 200 hexagonal mesh or lacey/carbon film, 200 quadratic mesh, both ScienceServices GmbH). The TEM grids were dried in air and mounted on a model 2020 tomography holder (Fischione Instruments). Due to synthetically based chemical and structural inhomogeneities in the carbon support the nucleation and growth behaviour of the nanoparticles may differ slightly depending on the carbon primary particle. Therefore, a minimum of 2000 nanoparticles on at least 10 carbon particles per sample were considered to enable quantitative conclusions. Nanoparticle size distributions for each sample were determined via ImageJ 1.53c. Tilt series were acquired automatically over a 140-144° tilt range (± 70-72°, 1° tilt increment) in STEM imaging mode with a beam current of ~50 pA and a convergence angle of ~9 mrad using the tomography STEM software V4.20. The collected Bright-field (BF) and high-angle annular dark-field (HAADF) image pairs (1024x1024 pixels, 15 µs dwell time) were binned by a factor of 2 and aligned by cross-correlation using Inspect3D. Energy dispersive X-ray (EDX) mappings were acquired in STEM-mode with a field of view of 100 nm. The acquisition was performed with 100 scans and 10 µs dwell time per scan (total acquisition time ~20 min).

Aberration-corrected STEM (Cs-STEM) micrographs were acquired using a JEM-ARM200CF (JEOL Ltd., Cold FEG emitter) at 80 kV acceleration voltage with a convergence angle of 25 mrad. Interplanar distances were determined with ImageJ by using a broad line scan to obtain the averaged grey value of the particles over the distance. Due to the overlap of some particles

with other particles in the background and the increase of the grey value with increasing particle thickness towards the particle core, the mean grey value was compensated accordingly.

2.2.4 Scanning electron microscopy (SEM)

The catalyst layer thickness was determined via SEM micrographs of cryo-cut cross-sections of the MEAs. The samples were cut in liquid nitrogen and mounted on standard aluminium 90° SEM Stubs (ScienceServices GmbH) with conductive double-sided adhesive carbon tabs. The SEM micrographs were acquired using a FE-SEM Amber X (Tescan GmbH) equipped with a secondary electron detector (Everhart-Thornley type). All micrographs were acquired at a working distance of approximately 6 mm using an acceleration voltage of 2 kV and a beam current of 100 pA. SEM micrographs and additional information regarding the measurement are presented in the Supporting Information (SI).

2.2.5 Thin-film rotating disk electrode

Oxygen reduction reaction (ORR) polarization curves and carbon monoxide (CO) electrooxidation cyclic voltammetry (CV) were measured in a thin-film rotating disk electrode (TF-RDE), of which the setup was described in the previous works.[26, 29]

As a reference electrode (RE), the reversible hydrogen electrode (RHE; HydroFlex, Gaskatel) was used, while the graphite rode electrode was used as a counter electrode. The working electrode (WE) was a 0.196 cm² glassy carbon disc embedded in Teflon (Pine Instruments). The WE was prepared following the procedure, which was also reported in the previous work:[29]

- Polishing to a mirror finish with Al_2O_3 paste (particle size 0.05 µm, Buehler) on a polishing cloth (Buehler)
- Rinsing and ultrasonication (Ultrasound bath Iskra Sonis 4) in Milli-Q water for 5 min
- Pipetting 20 µl of a freshly prepared water-based catalyst ink (1 $mg_{catalyst}$ per 1 $ml_{Milli\text{-}Q\ water}$) on the WE so that the WE is completely covered by the dispersion
- After the drop had dried, 5 µl of Nafion solution (EelctroChem, 5 % aqueous solution) diluted in isopropanol (1:50 v/v) was added to the WE with the catalyst ink to bind the catalyst thin-film on the glassy carbon electrode

After preparing the WE, it was mounted on the rotator (Pine Instruments). The RDE measurements performed in 0.1 M $HClO_4$ are as follows: ORR polarization curves were measured in an oxygen saturated electrolyte with rotation at 1600 rpm between 0.05 – 1.0 V_{RHE} with a scan rate of 20 mV s^{-1}. After the ORR polarization curve measurement, the electrolyte (0.1 M $HClO_4$) was purged with carbon monoxide (CO) under potentiostatic mode (0.05 V_{RHE}) for CO-stripping experiments, followed by Ar to saturate the electrolyte. CO-electrooxidation ("stripping") was performed using the same potential window (0.05 – 1.0 V_{RHE}) and scan rate (20 mV s^{-1}) as in ORR polarization curves, but without rotation and in an Ar-saturated electrode.[30]

Kinetics parameters from RDE experiments were calculated at 0.9 V_{RHE} with Koutecky-Levich equation, as described in literature[31, 32]

$$i^{-1} = i_{\mathrm{k}}^{-1} + i_{\mathrm{d}}^{-1} \quad (1)$$

Where i is the measured current density, i_k is the kinetic current and i_d is the diffusion limited current. From the kinetic current, the mass activity (MA) can be obtained by normalizing the

kinetic current i_k with the electrode area A_{Geo} (0.194 cm²) and the Pt loading L_{Pt} (20 µg / 0.196 cm² ≈ 0.1 mg_{Pt} cm^{-2}):

$$MA = \frac{i_k}{A_{Geo} \cdot L_{Pt}} \quad (2)$$

The ECSA was determined by integrating the charge in CO electrooxidation experiments between 0.4 V_{RHE} and 1.0 V_{RHE}, following the approach reported in literature.[30, 31]

2.3 Fabrication of Membrane Electrode Assemblies

The novel PtCo/C catalyst was prepared by ReCatalyst. The commercial PtCo/C catalyst was purchased from Umicore N.V. 3M PFSA ionomer was supplied by 3M and PFSA FS715RFS membranes were supplied by Fumatech BWT GmbH.

Anode catalyst inks (2 wt% solids in 1:4 w/w IPA/water) were prepared using Pt/C (45 wt% Pt content, Elyst Pt50 0550, Umicore) and an ionomer-to-carbon ratio (I/C) of 0.7. Three cathode catalyst inks (2 wt% solids in 1:4 w/w IPA/water) were prepared using three different catalysts; PtCo/C (35 wt% Pt content provided by ReCatalyst). As references, two commercial PtCo/C from Umicore were chosen: Elyst Pt50 0690 (41 wt% Pt content) and Elyst Pt30 0690 (27 wt% Pt content), as these are the common commercial PtCo/C reported in literature[33–35] and are commercially available with comparable metal content to the ReCatalyst catalyst. The membrane electrode assemblies (MEA) with the PtCo/C from ReCatalyst are denoted **ReCatalyst**. The references MEAs with PtCo/C from Umicore are denoted **UM50** for Elyst Pt50 0690 and **UM30** for Elyst Pt30 0690. The ionomer-to-carbon (I/C) ratio was adjusted to 0.4 for all cathodes, based on previously published work from our group.[36]

The catalyst layers were applied onto pristine membranes using an automated ultrasonic spray-coating system (Sonaer Sono-Cell). Anode and cathode catalyst inks were applied onto commercial Fumapem® membrane (725 EW, mechanically reinforced, chemically stabilized, nominal thickness: 15 µm). The desired Pt-loading of all MEAs was 0.1 mg·cm^{-2} for the anode and two different loadings for the cathode: 0.25 mg·cm^{-2} and 0.4 mg·cm^{-2}. The loading was controlled by weighing a thin metal pad of 2 cm² area before and after the spraying with a microbalance (ME36S, Satorius AG), as reported in a previous study.[37] The resulting catalyst-coated membranes were sandwiched between two 4 cm² gas diffusion layers (H14CX653, Freudenberg). The performances of the 4 cm² active area MEAs were evaluated using a fuel cell test station (Scribner 850e). All MEAs were tested with the same experimental protocol.

2.4 Characterization of Membrane Electrode Assemblies

The protocol applied to all the MEAs in this work consisted of a break-in procedure followed by voltage recovery (VR). This procedure was shown to be a valuable step for removing sulfate, which improves the electrochemical performance.[33, 38] After the voltage recovery, polarization measurements were conducted in H_2/O_2, followed by cyclic voltammograms for the determination of electrochemical active area (ECSA) and a hydrogen cross-over measurement for a proper mass activity assessment. Lastly, polarization measurements in H_2/air were performed.

The break-in procedure was reported in our previous work.[36] The voltage recovery protocol is based on the works of Zhang *et al*.[39] and Kabir *et al.*[33] During the VR, the cells were held under 55 °C, above saturation (198 % RH) and ambient pressure. A series of potential

cycles between 0.08 V and 0.12 V was applied for 20 s each on the cells. The voltage cycles were repeated 180 times.

The H_2/O_2 polarization curves (0.25 slpm/1 slpm) were measured under 80 °C, 96 % RH and 150 kPa_{abs}. The current density was scanned from 0 mA cm^{-2} to 125 mA cm^{-2} in 5 mA cm^{-2} steps for 5 minutes per point (average of last 5 seconds used). High-frequency resistances (HFRs) were measured at a frequency of 3200 Hz by the fuel cell test station's integrated Frequency Resistance Analyzer (FRA) throughout all polarization characterizations and used to correct for membrane, contact, and electronic resistances, as previously reported in our work.[36]

The Tafel plots were corrected for the high-frequency resistances (HFR) and the hydrogen cross-over current densities following the approach by Neyerlin *et al.*[40] The mass activity is obtained by dividing the current density corrected with hydrogen cross-over ($i + i_{x\text{-}over}$) at 0.9 $V_{HFR\text{-}free}$ with the cathode Pt-loading of the cell (0.25 mg_{Pt} cm^{-2}).

The cyclic voltammograms (CVs) were performed under H_2/N_2, 35 °C, 95 % RH and ambient pressure. The potential was swept from 0.05 to 1.0 V versus RHE at a scan rate of 50 mV s^{-1}. The CVs were repeated 8 times to reach saturation. The factor used to calculate the ECSA from the H_{upd} charge was 210 µC cm^{-2}, as reported in the literature.[33, 36] The cyclic voltammograms of the three samples are provided in the Supplementary Information (SI). We acknowledge that the hydrogen underpotential deposition (H_{upd}) method for Pt-alloy complicates the quantitative ECSA measurement due to the altered electronic properties of PtCo as this change affects the adsorption behaviour of hydrogen.[41, 42] The more accurate values for the ECSA are obtained by CO-stripping (see section 2.2.5), as the adsorption of CO is less affected by the altered electronic properties of PtCo.[42] However, differences in ECSAs will be discussed in section 3.2.1).

Hydrogen crossover currents were measured via linear sweep voltammetry (LSV) under H_2/N_2, and else, under the same conditions as the H_2/O_2 polarization curves, *i.e.* 80 °C, 96 % RH and 150 kPa_{abs} to correct the current densities from the H_2/O_2 polarization curves.

The H_2/air polarization curves (0.25 slpm/0.5 slpm) was measured at 80 °C and under two different conditions: a) 96 % RH and ambient pressure and b) 50 % RH and 250 kPa_{abs}. The current density was scanned from zero to 250 mA cm^{-2} in 12.5 mA cm^{-2} increments with a 1-minute hold at each current step.[36] Full polarization curves were obtained by scanning the current density from 375 mA cm^{-2} to 6250 mA cm^{-2} in 125 mA cm^{-2} increments with a 3-minute hold per current step.[36]

3 Results and Discussion

3.1 Particle composition and morphology

ICP-OES measurements revealed the Pt:Co compositions of the three catalysts to be $Pt_{2.8}Co$ for Umicore Elyst Pt30 0690 (UM30), $Pt_{2.4}Co$ for Elyst Pt50 0690 (UM50) and $Pt_{2.9}Co$ for PtCo/C synthesized via double-passivation galvanic displacement (ReCatalyst). XRD patterns of all three samples (Fig. 1) confirm the high-crystallinity and bimetallic alloy nature of all PtCo/C catalysts, whereby both are also evidenced by aberration-corrected STEM and STEM-EDX element mapping (Fig. S1 and S2), respectively. The diffractograms suggest the close similarity of the bulk chemical composition as well as the crystal structure of the as-

prepared ReCatalyst and PtCo/C references from Umicore. The diffraction peaks at 2θ = 24-26°, 33-34°, 40.9-41.3°, 47.6-47.9° and 54° correspond to the (001), (110), (111), (200) and (201) planes of intermetallic tetragonal *P4/mmm* PtCo. The peak at 2θ = 24-26° is superimposed by the (002) plane of the carbon support.[43] Compared to standard *face-centred cubic* (fcc) platinum, the dominant (111) and (200) plane peaks (denoted by the dashed lines, PDF(Pt)#00-004-0802) are shifted to higher 2θ values, indicating a substantial lattice contraction due to the formation of the alloy. Employing Bragg's law, interplanar spacings of 2.25 Å (UM30), 2.20 Å (UM50), and 2.21 Å (ReCatalyst) for the (111) plane and 3.80 Å (UM30), 3.82 Å (UM50), and 3.82 Å (ReCatalyst) for the (200) plane were obtained.[44] Measurements of interplanar distances of individual particles in the Cs-STEM micrographs yielded d-spacings averaging 2.23 Å and 3.84 Å for ReCatalyst, 2.19 Å and 3.80 Å for UM50 and 2.22 Å for UM30 (Fig. S3), closely matching the values found by diffractometry. These values are approximately in agreement with d-spacings of PtCo alloys reported in the literature and are slightly shortened compared to the d-spacings reported for pure platinum nanoparticles (~2.3 Å and ~3.9-4.0 Å, respectively).[45–49]

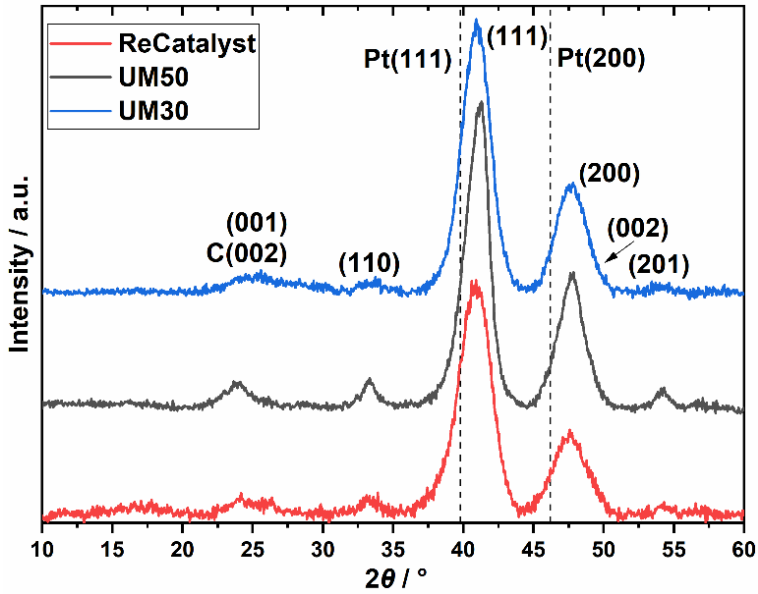

Figure 1: X-Ray diffraction patterns of the ReCatalyst (PtCo/C synthesized via galvanic displacement, red) and the two benchmark catalysts Umicore UM30 (blue) and UM50 (black).

The observed lattice distance decrease could result from the incorporation of the smaller cobalt atoms (atomic radius of 1.26 Å) in place of the larger platinum atoms (1.36 Å).[50, 51] The pronounced broadening of these reflections in all three samples suggests a small mean crystallite size. As the width of a diffraction peak is not only influenced by the crystallite size, but also by crystal lattice imperfections such as dislocations, chemical inhomogeneities and residual stress, it is not advised to calculate specific crystallite size values (e.g. by the often used Scherrer equation[52]) by simply measuring the full width at half maximum (FWHM).[53] Nevertheless, a decreasing FWHM was observed in order of UM50 (2.0°) < UM30 (2.4°) < ReCatalyst (2.7°) for the (111) plane, suggesting a slightly larger crystallite size for the Umicore references. To obtain more precise information about the particle morphology, additional TEM micrographs over a larger field of view were acquired (Fig. 2, more micrographs can be found

in Fig. S4-6). The carbon support in all three samples consists of 30-80 nm primary carbon particles, which coalesce into aggregates. These primary carbon particles are characterized by core-filling amorphous and shell-like graphitic carbon (see more resolved HRTEM micrographs in Fig. S7). The resemblance of the carbon support in all samples, as well as the similarity of the XRD patterns and former findings in their electrochemical behaviour confirms that the Umicore references also contain a high surface area carbon as support material.[26] It can be seen that on all samples, the PtCo nanoparticles are finely distributed over the entire carbon surface. From 2D TEM micrographs it is not possible to determine the precise proportion of nanoparticles located inside or outside the carbon pores. As proposed by Harzer *et al.*, however, some nanoparticles can be reliably assigned to be on the outside of the carbon support if the nanoparticle is clearly visible outside the projection of the carbon primary particle. In turn, it cannot be resolved whether a particle sits on the surface or in a carbon pore if that nanoparticle is completely enclosed by the projection of the primary carbon particle.[54]

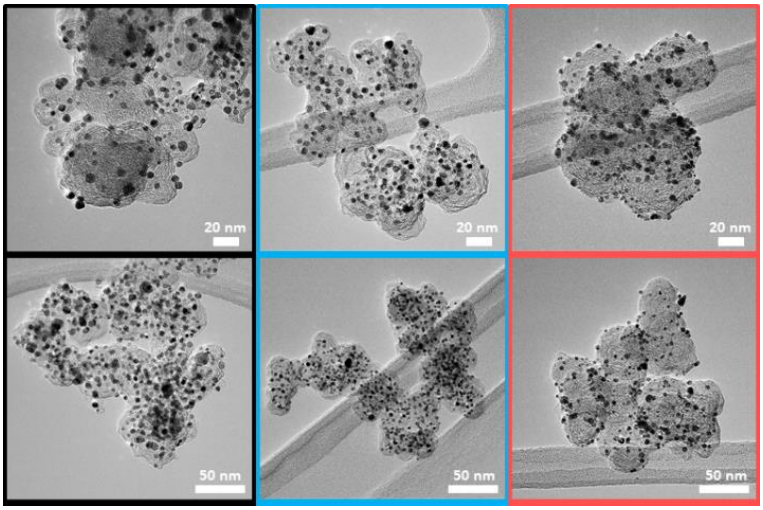

Figure 2: Representive TEM micrographs of the three catalysts UM50 (black), UM30 (blue) and ReCatalyst (red).

With this counting method, it can be estimated that more nanoparticles are located on the carbon surface for the ReCatalyst compared to the Umicore catalysts, as notably more particles are located outside the carbon projections. This is supported by TEM tilt series (Suppl. movies 1-3), where the rotation of the respective carbon particles over a wide tilt range (typically 140-144°) allows a better determination of the nanoparticle position.

A main advantage of the developed synthesis route is the narrower particle size distribution, which in general could be considered as advantageous towards the reduction of excessive Ostwald ripening of the particles upon aging.[55] Fig. 3 shows a violin plot with the particle size distribution obtained by measuring the diameters of the nanoparticles in the 2D TEM micrographs.

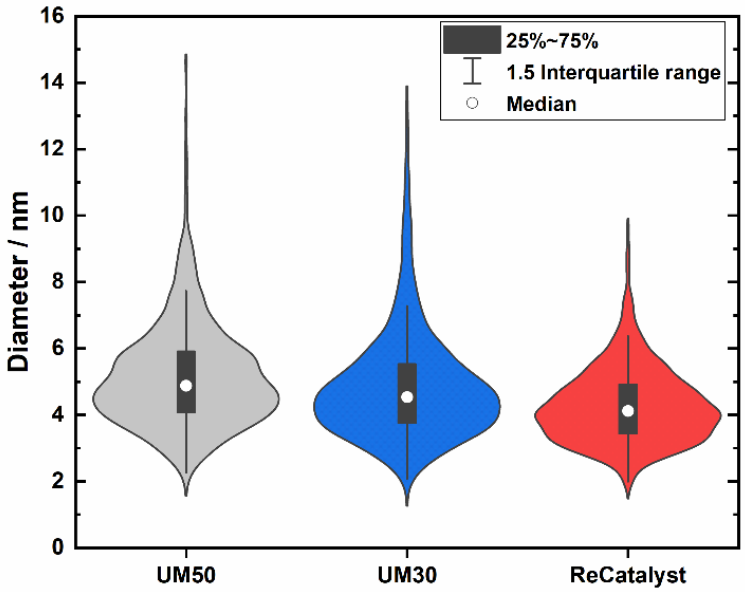

Figure 3*:* Violin plots of the particle size distribution for the three PtCo/C catalysts.

The vast majority of the measured nanoparticles for all three samples feature a diameter of 3 to 6 nm. The number-weighted diameter was determined to be 4.8 nm for UM50, 4.5 nm for UM30 and 4.1 nm for ReCatalyst, while the surface normalized diameters were calculated to be 6.3 nm for UM50, 6.1 nm for UM30 and 5.1 nm for ReCatalyst, respectively.[54] In comparison, a diameter of ~4.4 nm was reported for the Umicore Elyst Pt 50 0670 variant.[56,57] Following Schulenburgs' *et al.* approach for more realistic determinations of the surface area by TEM micrograph evaluation, we approximated the TEM derived surface areas of the samples to be 68 $m^2g_{Pt}^{-1}$ for UM50, 75 $m^2g_{Pt}^{-1}$ for UM30 and 86 $m^2g_{Pt}^{-1}$ for ReCatalyst assuming spherical particles.[41] It is important to note that although the majority of nanoparticles have comparable diameters, it is the significantly smaller number of particularly large (>8 nm) nanoparticles in the ReCatalyst sample that plays a crucial role in the utilization of the employed precious metal, which is directly quantified by the ECSA (see Fig. 5 and S8-S10 for detailed histograms of the particle size distributions). While the surface area of the ReCatalyst catalyst from purely geometric considerations is already 26 % and 17 % higher compared to UM30 and UM50, respectively, these differences are substantially greater for the electrochemical surface area. These differences are discussed in section 3.3. Both size and geometry are fundamentally determinating the active sites of the particles (besides the chemical composition) and thus influence the critical selectivity and stability of the catalyst.[58] This is called the particle size effect where smaller particles exhibited lower specific ORR activity and lower stability.[58–60] To not underutilize precious metal in the bulk of the particle and risk mass activity losses, it is essential to ensure large enough diameters that allow electrochemical activity and sufficient stability of the particles, but at the same time show a high surface-to-volume ratio for electrochemical surface maximization. These relationships have been extensively modelled and experimentally investigated for the simpler Pt/C system, where Pt nanoparticles with diameters of ~2-4 nm have been determined to feature optimal mass activity.[61–64] Even though particle size studies of PtCo nanoparticles are not similarly extensive and are more difficult to obtain due to the alloy nature of nanoparticles with varying intraparticle elemental (e.g. Pt/Co ratio) and structural (e.g. degree of ordering) compositions, similar trends seem to apply.[20, 65, 66] E.g.

according to Wang *et al.* the maximum mass activity for Pt_3Co nanoparticles is found at particle sizes of ~4.5 nm, although it must be pointed out that this activity also depends strongly on numerous other parameters (e.g. element composition, particle shape).[67, 68] In Fig. 4, the highest mass fraction for ReCatalyst is found at 4-5 nm, which lies in this optimal range for catalyst activity. For the commercial catalysts, the distribution is slightly shifted to 5-6 nm. This trend is in line with the improvement in RDE derived ECSA and mass activity of the ReCatalyst material compared to the UM references (see below, Fig. S11+12 and Table S1).

A second important factor influencing the catalyst performance is the loss of active catalyst material in large catalyst particles: For assumed solid spherical particles with a diameter of 6 nm or more, more material is found inside the particle than at the surface marking the lower limit above which the proportion of inside and outside material inflects, due to spheres having the lowest surface to volume ratio. In nature, nanoparticles are not perfectly spherical and not only the first atomic surface layer but also the subsequent atomic layers below have a crucial influence on the reaction, as shown with DFT calculations by Patrick *et al.*, albeit with decreasing significance.[15] It can be expected that above a particle size of ~8 nm the majority of the core atoms play a negligible role in the oxygen reduction reaction and thus the contribution of the fractional mass activity of these particles to the total mass activity of the catalyst is almost zero. Applying this consideration to the analysis of our TEM investigation summarized in the binned histogram in Fig. 4 (binned values in Table S2), we find a significantly reduced mass ratio of particles > 8 nm for the ReCatalyst (~10 %) vs. the Umicore references (~26 % and 35 % for Umicore 50 and 30, respectively). This finding clearly confirms the advantage of the alternative fabrication procedure given the sharper particle size distribution for the ReCatalyst material.[24–26] Nevertheless, one can assume considerable benefits are still accessible with further optimization of the particle size distribution if a complete elimination of particles with diameters > 8 nm is achieved. The mass fraction of particles < 3 nm is very low in all three samples (below ~2.5 % for all samples). Since very small particles feature a strong curvature, they are prone to faster decomposition due to increased surface energy and are therefore unfavourable for catalyst long-term durability.[69, 70] We also acknowledge, however, that the detection of nanoparticles in the sub-nm range is difficult due to the acquisition of TEM micrographs with an intermediate field of view (typically 50-200 nm) with associated reduced pixel resolution, which could be circumvented by improved imaging equipment in future work.

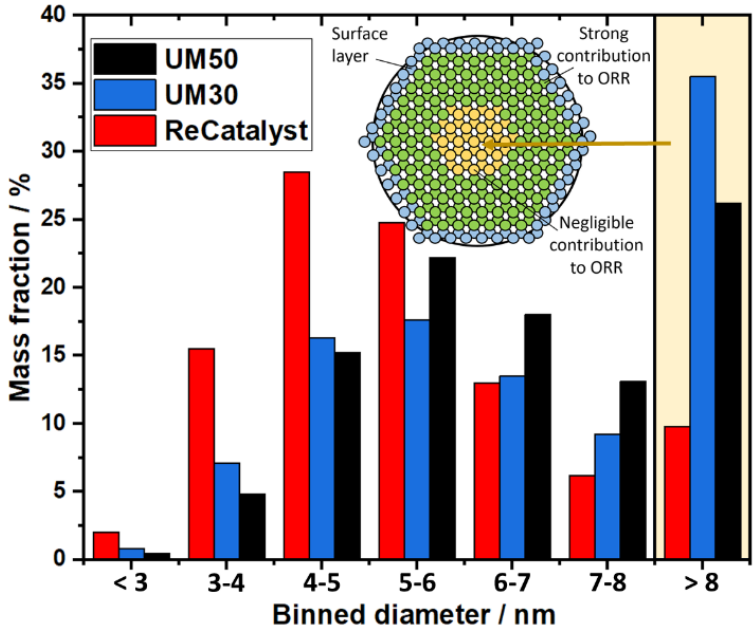

Figure 4*:* Mass distribution of the three PtCo/C catalysts.

3.2 Electrochemical performance

Given the different size distribution of the three catalysts, the following sections show the concomitant ECSA (section 3.2.1) and catalytic activity (section 3.2.2) of the samples.

3.2.1 Electrochemical surface area

Fig. 5 shows the ECSA of the three catalysts. The same trend of ECSA was observed independent of the measurement method: the ECSA, or the concomitant roughness factor of the ReCatalyst PtCo/C is higher than the two references UM50 and UM30 (Fig. 5). The higher ECSA of the ReCatalyst PtCo/C correlates well with the narrower particle size distribution discussed above, leading to a greater total active surface area. Further information obtained from the in situ CVs is shown in Fig. S13.

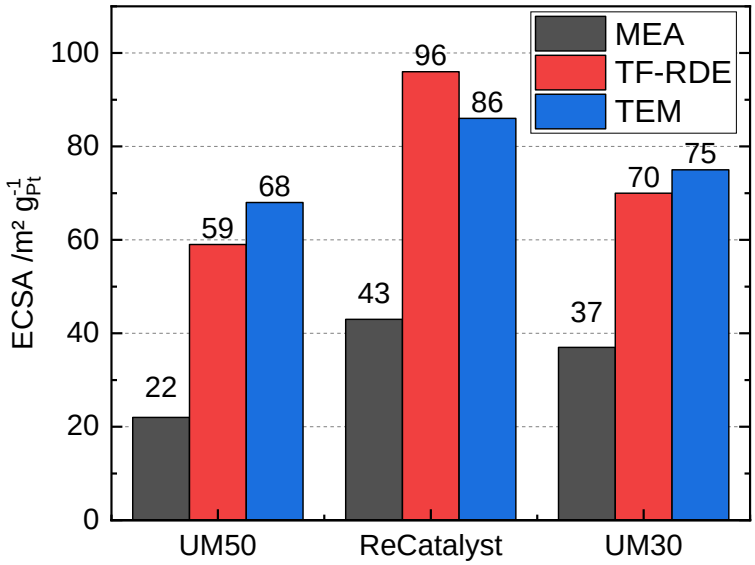

Figure 5: Electrochemical active surface area of three catalysts obtained by H_{upd} in MEA setup and CO-stripping with thin-film RDE. The estimated available surface was determined by TEM measurements.

The ECSAs of all samples measured with CO-stripping in the thin-film rotating disk electrode (TF-RDE) setup is at least 1.9 times higher than those obtained with H_{upd} in the MEA setup, which is similar to the results reported in the literature.[31, 42, 71] We are aware that the H_{upd} for Pt-alloy only serves as indicative values due to the altered electronic properties of PtCo, which affects the adsorption behavious of hydrogen more than of CO. Still, the qualitative comparison between the three samples confirms the observed trend in ECSA values, measured by TEM and TF-RDE.

3.2.2 In-situ electrochemical performance

In the MEA all three catalysts showed comparable mass activities: ReCatalyst PtCo/C (150 ± 2 mA mg_{Pt}^{-1}) ranges between that of UM50 (130 ± 3 mA mg_{Pt}^{-1}) and UM30 (170 ± 4 mA mg_{Pt}^{-1}). The Tafel plots and the corresponding mass specific current density are presented in Fig. S14 and S15. It was observed in thin-film rotating disk electrode (TF-RDE) measurements, that the mass activity of ReCatalyst PtCo/C (2 A mg_{Pt}^{-1}) was > 2x higher than the reference catalysts (0.7 A mg_{Pt}^{-1} for UM50 and 0.8 A mg_{Pt}^{-1} for UM30, Table S1). As it is most likely that ReCatalyst PtCo/C features a higher fraction of exterior PtCo on carbon than the references (as discussed earlier), the chance for ionomer-induced poisoning for ReCatalyst catalyst is higher compared to the UM catalysts.[72–75] This hypothesis is further supported by other prior fundamental studies in the liquid electrolyte by N. Marković *et al.* on single crystal surfaces of Pt.[76, 77] The authors have shown that the variations in activity for oxygen reduction with crystal facets arise from the different structural sensitivity on the adsorption of anions in the electrolyte. In this sense, the sulfate anions, which are also presented in the ionomer, have been shown to more strongly interact with the most active (111) facet and can significantly inhibit the activity (catalyst poisoning). Since the TF-RDE measurements were performed in 0.1 M $HClO_4$, for the kinetic performance of the ReCatalyst PtCo/C catalyst, the position of the nanoparticles did not play as a significant role as in the MEA. While further investigation is

required, this could explain the observed discrepancy between the kinetic performance (mass activity) of ReCatalyst PtCo/C obtained by TF-RDE (Table S1) and on the MEA level.

The polarization curves of the MEAs with the three catalysts are shown in Figure 6 (H_2/air, 80 °C, 96 % RH, ambient pressure) and Figure 7 (H2/air, 80 °C, 50 % RH, 250 kPa_{abs}). It can be seen that in particular at high current densities (> 750 mA cm^{-2}), the MEA performance with ReCatalyst is superior in both operating conditions at the same Pt loadings. This is most likely linked to the significantly higher ECSA (Fig. 5) and probably also to a higher fraction of exterior PtCo particles on carbon (as discussed earlier), which can improve the mass transport, *e.g.* by improved accessibility to oxygen, especially at high current densities.[5, 78] This result confirms the trade-off between the ionomer-induced positioning of the catalyst nanoparticles and achieved kinetic performances in the MEA and on the other hand, the mass transport properties and accessibility of the Pt nanoparticles to enable high current densities, as presented in a highly regarded publication by Yarlagada *et al.*[79] In addition, these results highlight how nano-engineering/tailoring of the catalyst is critical and how high kinetic performances in TF-RDE do not predict the behaviour one can expect in the entire current range in an MEA.

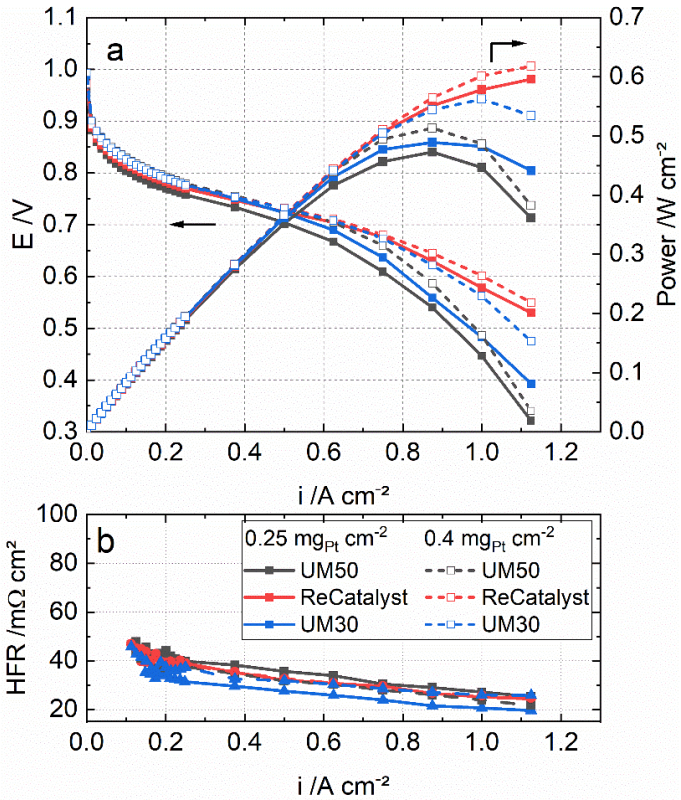

Figure 6: Polarization curves (a) and the high-frequency resistances (b) of the MEAs with UM50, ReCatalyst and UM30 at 0.25 mg_{Pt} cm^{-2} loading and 0.4 mg_{Pt} cm^{-2} loading under H_2/air, 80 °C, 95 % RH.

Figure 6 and Figure 7 also shows the comparison of the MEAs with the three catalysts in two different cathode loadings: 0.4 mg_{Pt} cm^{-2} and 0.25 mg_{Pt} cm^{-2}. It can be seen that the performance of the ReCatalyst MEA is not affected much by the reduced loading. Even with a lower Pt loading, the MEA with 0.25 mg_{Pt} cm^{-2} ReCatalyst PtCo/C in the cathode CL still outperforms that with 0.4 mg_{Pt} cm^{-2} UM50 in both conditions. This result indicates that the

higher peak performance of the ReCatalyst MEA (0.25 mg_{Pt} cm^{-2}) is mainly accounted to the greater ECSA and the concomitant surface roughness (the product of Pt loading and ECSA)[78] in combination with a possibly higher fraction of exterior PtCo on carbon than the references which improves the oxygen assessment to the Pt surface at high current densities.[5, 78] In addition, this improvement is not captured with the catalyst layer thicknesses, as these are similar for both catalyst layers with UM50 at 0.4 mg_{Pt} cm^{-2} and ReCatalyst at 0.25 mg_{Pt} cm^{-2} (both are approx. 10 µm, Fig. S16). Under H_2/air, 96 % RH, ambient pressure (Figure 6), the performance of ReCatalyst MEA was reduced only by 4 % at 0.7 V and peak power density (PPD) when the Pt-loading was reduced from 0.4 to 0.25 mg_{Pt} cm^{-2}. The performance of the UM50 MEA (-20 % at 0.7 V and -8 % at PPD) and UM30 MEA (-10 % at 0.7 V and -14 % at PPD) was reduced more than the ReCatalyst MEA when the Pt loading was reduced from 0.4 to 0.25 mg_{Pt} cm^{-2}. The identical trend was measured under another different operation condition (H_2/air, 50 % RH, 250 kPa_{abs}). The performance of the lower loading (0.25 mg cm^{-2}) ReCatalyst MEA under the given condition was reduced by 13 % at 0.7 V and only 6 % at PPD from that of the higher loading (0.4 mg cm^{-2}), while the performance of the lower loading UM50 cell was reduced by 24 % at 0.7 V and 17 % at PPD. The performance at 0.7 V of the lower loading UM30 cell under the given conditions was almost unaffected (reduction by 1 %), but the performance at PPD was reduced by 10 % from its higher loading equivalent. The lower reduction in performance with the decreasing loading is as well an expected outcome from the previously described results on the higher ECSA of ReCatalyst PtCo/C.[78, 79]

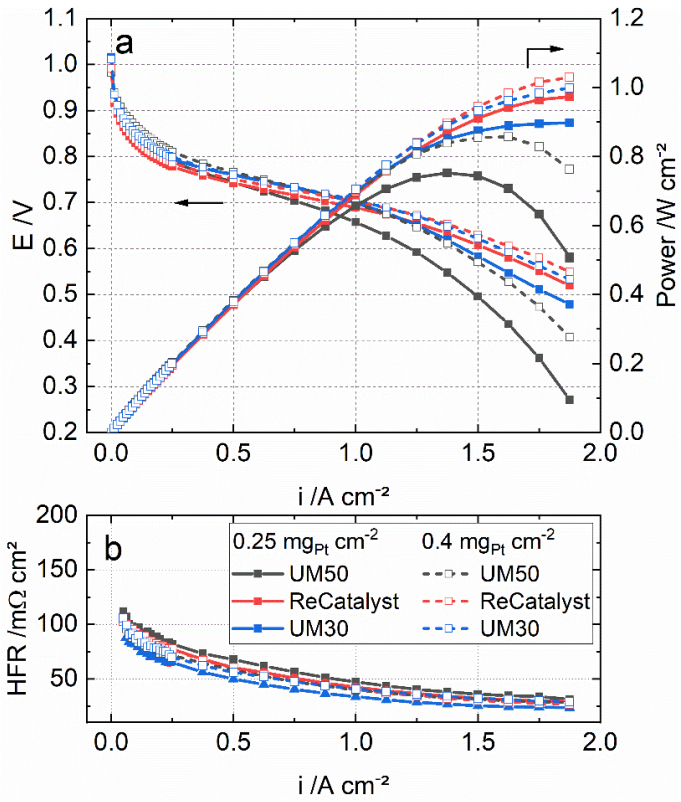

Figure 7: Polarization curves (a) and the high-frequency resistances (b) of the MEAs with UM50, ReCatalyst and UM30 at 0.25 mg_{Pt} cm^{-2} loading and 0.4 mg_{Pt} cm^{-2} loading under H_2/air, 80 °C, 50 % RH and 250 kPa_{abs}.

4 Conclusion

Based on an alternative catalyst synthesis approach via the double passivation galvanic displacement, we have shown that a significantly narrowed particle size distribution can be obtained. By TEM and XRD characterization we were able to show that the novel ReCatalyst PtCo/C features a considerably lower mass fraction of particles > 8 nm vs. two competitive commercial references. In addition, more nanoparticles are located on the carbon surface for the ReCatalyst compared to the Umicore catalysts. These two features enable more effective usage of the available active catalyst material, which is reflected in single-cell characterization, especially at high current densities and reduced Pt-loading (0.25 mg_{Pt} cm^{-2}). We were able to obtain significantly higher cell performances (~ 1 W cm^{-2} at 0.55 V under H_2/air, 50 % RH, 250 kPa_{abs}) compared to the references (< 0.9 W cm^{-2} at the same potential and the given conditions). Future works should aim at further optimization of this new catalyst system in MEAs, in particular, closing the herein observed gap between RDE and MEA mass activity values to finally exploit the full potential of those novel catalysts.

Conflict of interest

The authors declare no competing financial interest.

Acknowledgements

The authors acknowledge funding from the Federal Ministry of Education and Research of Germany (BMBF) within the project FC-CAT (Grant 08SF0579B) and the Federal Ministry for Economic Affairs and Energy (BMWi) within the project DirectStack (Grant O3ETBO24D). We would also like to thank the Slovenian research agency (ARRS) programs P2-0393, P1-0034; the projects NC-0007, NC-0016 and N2-0106; NATO Science for Peace and Security Program under Grant G5729; and European Research Council (ERC) Starting Grant 123STABLE (Grant agreement ID: 852208) and Proof of Concept Grant StableCat (Grant agreement ID: 966654) for funding the study. The authors would like to thank Ralf Thomann for valuable discussions concerning TEM imaging. The authors would like to acknowledge Mark Muggli from 3M for providing PFSA ionomer and Fumatech for providing PFSA membrane.

References

1. M. K. Debe, *Nature,* **486**(7401), 43–51 (2012).
2. T. Yoshida and K. Kojima, *Electrochem. Soc. Interface,* **2015,** 45 (24).
3. A. Wilson, G. Kleen and D. Papageorgopoulos, *DOE Fuel Cell Technologies Office Record 17007: Fuel Cell System Cost – 2017 (*2017).
4. C. S. Gittleman, A. Kongkanand, D. Masten and W. Gu, *Curr. Opin. Electrochem.,* **18,** 81–89 (2019).
5. J. Fan, M. Chen, Z. Zhao, Z. Zhang, S. Ye, S. Xu, H. Wang and H. Li, *Nat. Energy,* **6**(5), 475–486 (2021).
6. D. Wang, H. L. Xin, R. Hovden, H. Wang, Y. Yu, D. A. Muller, F. J. DiSalvo and H. D. Abruña, *Nat. Mater.,* **12**(1), 81–87 (2013).
7. L. Bu, S. Guo, X. Zhang, X. Shen, D. Su, G. Lu, X. Zhu, J. Yao, J. Guo and X. Huang, *Nat. Comm.,* **7,** 11850 (2016).

8. D. S. Choi, A. W. Robertson, J. H. Warner, S. O. Kim and H. Kim, *Adv. Mater.,* **28**(33), 7115–7122 (2016).
9. S. B. Barim, S. E. Bozbag, B. Deljoo, M. Aindow and C. Erkey, *Fuel Cells,* **20**(3), 285–299 (2020).
10. P. Strasser, S. Koh, T. Anniyev, J. Greeley, K. More, C. Yu, Z. Liu, S. Kaya, D. Nordlund, H. Ogasawara, M. F. Toney and A. Nilsson, *Nat. Chem.,* **2**(6), 454–460 (2010).
11. X. Cai, R. Lin, D. Shen and Y. Zhu, *ACS applied materials & interfaces,* **11**(33), 29689–29697 (2019).
12. V. R. Stamenkovic, B. Fowler, B. S. Mun, G. Wang, P. N. Ross, C. A. Lucas and N. M. Marković, *Science,* **315**(5811), 493–497 (2007).
13. M. Pourbaix, *Atlas of Electrochemical Equilibria in Aqueous Solutions,* NACE International (1974).
14. C. E. Carlton, S. Chen, P. J. Ferreira, L. F. Allard and Y. Shao-Horn, *J. Phys. Chem. Lett.,* **3**(2), 161–166 (2012).
15. B. Patrick, H. C. Ham, Y. Shao-Horn, L. F. Allard, G. S. Hwang and P. J. Ferreira, *Chem. Mater.,* **25**(4), 530–535 (2013).
16. S. Koh and P. Strasser, *J. Am. Chem. Soc.,* **129**(42), 12624–12625 (2007).
17. R. Srivastava, P. Mani, N. Hahn and P. Strasser, *Angew. Chem. Int. Ed.,* **46**(47), 8988–8991 (2007).
18. M. Gatalo, L. Moriau, U. Petek, F. Ruiz-Zepeda, M. Šala, M. Grom, T. Galun, P. Jovanovič, A. Pavlišič, M. Bele, N. Hodnik and M. Gaberšček, *Electrochim. Acta,* **306,** 377–386 (2019).
19. M. Gatalo, P. Jovanovič, U. Petek, M. Šala, V. S. Šelih, F. Ruiz-Zepeda, M. Bele, N. Hodnik and M. Gaberšček, *ACS Appl. Energy Mater.,* **2**(5), 3131–3141 (2019).
20. C. Zalitis, A. Kucernak, X. Lin and J. Sharman, *ACS Catal.,* **10**(7), 4361–4376 (2020).
21. F. Xiao, X. Qin, M. Xu, S. Zhu, L. Zhang, Y. Hong, S.-I. Choi, Q. Chang, Y. Xu, X. Pan and M. Shao, *ACS Catal.,* **9**(12), 11189–11198 (2019).
22. M. Ko, E. Padgett, V. Yarlagadda, A. Kongkanand and D. A. Muller, *J. Electrochem. Soc.,* **168**(2), 24512 (2021).
23. Y. Xiong, Y. Yang, H. Joress, E. Padgett, U. Gupta, V. Yarlagadda, D. N. Agyeman-Budu, X. Huang, T. E. Moylan, R. Zeng, A. Kongkanand, F. A. Escobedo, J. D. Brock, F. J. DiSalvo, D. A. Muller and H. D. Abruña, *Proceedings of the National Academy of Sciences of the United States of America,* **116**(6), 1974–1983 (2019).
24. M. Gatalo, M. Bele, F. Ruiz-Zepeda, E. Šest, M. Šala, A. R. Kamšek, N. Maselj, T. Galun, P. Jovanovič, N. Hodnik and M. Gaberšček, *Angew. Chem. Int. Ed.,* **58**(38), 13266–13270 (2019).
25. L. Pavko, M. Gatalo, G. Križan, J. Križan, K. Ehelebe, F. Ruiz-Zepeda, M. Šala, G. Dražić, M. Geuß, P. Kaiser, M. Bele, M. Kostelec, T. Đukić, N. van de Velde, I. Jerman, S. Cherevko, N. Hodnik, B. Genorio and M. Gaberšček, *ACS Appl. Energy Mater.,* **4**(12), 13819–13829 (2021).
26. T. Đukić, L. J. Moriau, L. Pavko, M. Kostelec, M. Prokop, F. Ruiz-Zepeda, M. Šala, G. Dražić, M. Gatalo and N. Hodnik, *ACS Catal.,* **12**(1), 101–115 (2022).
27. D. Myers, N. Kariuki, R. Ahluwalia, X. Wang and J.-K. Peng, *Rationally Designed Catalyst Layers for PEMFC Performance Optimization (*2015, PDF, retrieved 21.03.2022).
28. A. Kongkanand, R. Leach, D. Papageorgopoulos, G. Kleen, P. Strasser, R. O'Malley, Y. Shao-Horn, D. E. Ramaker and S. Mukerjee, *High-Activity Dealloyed Catalysts,* https://doi.org/10.2172/1262711 (2014).
29. N. Maselj, M. Gatalo, F. Ruiz-Zepeda, A. Kregar, P. Jovanovič, N. Hodnik and M. Gaberšček, *J. Electrochem. Soc.,* **167**(11), 114506 (2020).

30. M. Gatalo, A. Martinez Bonastre, L.-J. Moriau, H. Burdett, F. Ruiz-Zepeda, E. Hughes, A. Hodgkinson, M. Šala, L. Pavko, M. Bele, N. Hodnik, J. Sharman and M. Gaberšček (2022), DOI: 10.26434/chemrxiv-2022-ls3vz
31. K. Mayrhofer, D. Strmcnik, B. B. Blizanac, V. Stamenkovic, M. Arenz and N. M. Markovic, *Electrochim. Acta,* **53**(7), 3181–3188 (2008).
32. A. J. Bard and L. R. Faulkner, *Electrochemical methods: Fundamentals and applications*, Hoboken, NJ, Wiley (2001).
33. S. Kabir, D. J. Myers, N. Kariuki, J. Park, G. Wang, A. Baker, N. Macauley, R. Mukundan, K. L. More and K. C. Neyerlin, *ACS Appl. Mater. Interfaces,* **11**(48), 45016–45030 (2019).
34. T. van Cleve, G. Wang, M. Mooney, C. F. Cetinbas, N. Kariuki, J. Park, A. Farghaly, D. Myers and K. C. Neyerlin, *J. Power Sources,* **482,** 228889 (2021).
35. Y. Garsany, R. W. Atkinson, B. D. Gould and K. E. Swider-Lyons, *J. Power Sources,* **408**(1), 38–45 (2018).
36. H. T. T. Nguyen, F. Lombeck, C. Schwarz, P. A. Heizmann, M. Adamski, H.-F. Lee, B. Britton, S. Holdcroft, S. Vierrath and M. Breitwieser, *Sustain. Energy Fuels*(5), 3687–3699 (2021).
37. C. Klose, T. Saatkamp, A. Münchinger, L. Bohn, G. Titvinidze, M. Breitwieser, K.-D. Kreuer and S. Vierrath, *Adv. Energy Mater.,* **10**(14), 1903995 (2020).
38. J. Zhang, B. A. Litteer, F. D. Coms and R. Makharia, *J. Electrochem. Soc.,* **159**(7), F287-F293 (2012).
39. J. Zhang, L. Paine, A. Nayar and R. Makharia, *Methods and processes to recover voltage loss of PEM fuel cell stack* (US2011/0195324 A1) (Nov. 4, 2010).
40. K. C. Neyerlin, W. Gu, J. Jorne, A. Clark and H. A. Gasteiger, *J. Electrochem. Soc.,* **154**(2), B279 (2007).
41. H. Schulenburg, J. Durst, E. Müller, A. Wokaun and G. G. Scherer, *J. Electroanal. Chem.,* **642**(1), 52–60 (2010).
42. D. F. van der Vliet, C. Wang, D. Li, A. P. Paulikas, J. Greeley, R. B. Rankin, D. Strmcnik, D. Tripkovic, N. M. Markovic and V. R. Stamenkovic, *Angew. Chem.,* **124**(13), 3193–3196 (2012).
43. T. Kim and B. N. Popov, *Int. J. Hydrog. Energy,* **41**(3), 1828–1836 (2016).
44. W. H. Bragg and W. L. Bragg, *Proc. R. Soc. Lond. A.,* **1913**(88), 428–438 (193).
45. S. Dai, Y. You, S. Zhang, W. Cai, M. Xu, L. Xie, R. Wu, G. W. Graham and X. Pan, *Nat. Comm.,* **8**(1), 204 (2017).
46. K. Miyazawa, M. Yoshitake and Y. Tanaka, *J Nanopart Res,* **19**(6), F57 (2017).
47. J. Y. Song, E.-Y. Kwon and B. S. Kim, *Bioprocess and biosystems engineering,* **33**(1), 159–164 (2010).
48. C. Zhang, R. Zhang, X. Gao, C. Cheng, L. Hou, X. Li and W. Chen, *ACS Omega,* **3**(1), 96–105 (2018).
49. N. V. Long, M. Ohtaki, M. Uchida, R. Jalem, H. Hirata, N. D. Chien and M. Nogami, *Journal of colloid and interface science,* **359**(2), 339–350 (2011).
50. S.-I. Choi, S.-U. Lee, W. Y. Kim, R. Choi, K. Hong, K. M. Nam, S. W. Han and J. T. Park, *ACS applied materials & interfaces,* **4**(11), 6228–6234 (2012).
51. B. Cordero, V. Gómez, A. E. Platero-Prats, M. Revés, J. Echeverría, E. Cremades, F. Barragán and S. Alvarez, *Dalton transactions (Cambridge, England : 2003)*(21), 2832–2838 (2008).
52. P. Scherrer, *Göttinger Nachrichten Math. Phys.,* **1918**(2), 98–100 (1918).
53. J. I. Langford and A. Wilson, *J. Appl. Cryst.,* **1978**(11), 102–113.
54. G. S. Harzer, A. Orfanidi, H. El-Sayed, P. Madkikar and H. A. Gasteiger, *J. Electrochem. Soc.,* **165**(10), F770-F779 (2018).
55. M. Watanabe, H. Yano, H. Uchida and D. A. Tryk, *Journal of Electroanalytical Chemistry,* **819,** 359–364 (2018).

56. R. K. Ahluwalia, D. D. Papadias, N. Kariuki, J.-K. Peng, X. Wang, Y. Tsai, D. G. Graczyk and D. J. Myers, *Journal of The Electrochemical Society,* **2018**(265), F3024-F3035 (2018).
57. D. D. Papadias, R. K. Ahluwalia, N. Kariuki, D. J. Myers, K. L. More, D. A. Cullen, B. Sneed, K. C. Neyerlin, R. Mukundan and R. L. Borup, *Journal of The Electrochemical Society,* **2018**(165), F3166-F3177 (2018).
58. M. Nesselberger, S. Ashton, J. C. Meier, I. Katsounaros, K. J. J. Mayrhofer and M. Arenz, *Journal of the American Chemical Society,* **133**(43), 17428–17433 (2011).
59. F. J. Perez-Alonso, D. N. McCarthy, A. Nierhoff, P. Hernandez-Fernandez, C. Strebel, I. E. L. Stephens, J. H. Nielsen and I. Chorkendorff, *Angewandte Chemie (International ed. in English),* **51**(19), 4641–4643 (2012).
60. P. Jovanovič, U. Petek, N. Hodnik, F. Ruiz-Zepeda, M. Gatalo, M. Šala, V. S. Šelih, T. P. Fellinger and M. Gaberšček, *Physical chemistry chemical physics: PCCP,* **19**(32), 21446–21452 (2017).
61. Z. Xu, H. Zhang, H. Zhong, Q. Lu, Y. Wang and D. Su, *Applied Catalysis B: Environmental,* **111-112,** 264–270 (2012).
62. M. Shao, A. Peles and K. Shoemaker, *Nano letters,* **11**(9), 3714–3719 (2011).
63. K. Kinoshita, *Journal of The Electrochemical Society,* **1990**(137), 845 (1990).
64. G. A. Tritsaris, J. Greeley, J. Rossmeisl and J. K. Nørskov, *Catal Lett,* **141**(7), 909–913 (2011).
65. K. Matsutani, K. Hayakawa and T. Tada, *Platin Metals Rev. (Platinum Metals Review),* **54**(4), 223–232 (2010).
66. M. Gummalla, S. Ball, D. Condit, S. Rasouli, K. Yu, P. Ferreira, D. Myers and Z. Yang, *Catalysts,* **5**(2), 926–948 (2015).
67. C. Wang, D. van der Vliet, K.-C. Chang, H. You, D. Strmcnik, J. A. Schlueter, N. M. Markovic and V. R. Stamenkovic, *J. Phys. Chem. C,* **113**(45), 19365–19368 (2009).
68. C. Wang, G. Wang, D. van der Vliet, K.-C. Chang, N. M. Markovic and V. R. Stamenkovic, *Physical chemistry chemical physics : PCCP,* **12**(26), 6933–6939 (2010).
69. W. Sheng, S. Chen, E. Vescovo and Y. Shao-Horn, *Journal of The Electrochemical Society,* **2011**(159), B59 (2011).
70. J. C. Meier, C. Galeano, I. Katsounaros, J. Witte, H. J. Bongard, A. A. Topalov, C. Baldizzone, S. Mezzavilla, F. Schüth and K. J. J. Mayrhofer, *Beilstein journal of nanotechnology,* **5,** 44–67 (2014).
71. S. Rudi, C. Cui, L. Gan and P. Strasser, *Electrocatalysis,* **5**(4), 408–418 (2014).
72. K. Kodama, A. Shinohara, N. Hasegawa, K. Shinozaki, R. Jinnouchi, T. Suzuki, T. Hatanaka and Y. Morimoto, *J. Electrochem. Soc.,* **161**(5), F649-F652 (2014).
73. R. Jinnouchi, K. Kudo, K. Kodama, N. Kitano, T. Suzuki, S. Minami, K. Shinozaki, N. Hasegawa and A. Shinohara, *Nature communications,* **12**(1), 4956 (2021).
74. K. Kodama, K. Motobayashi, A. Shinohara, N. Hasegawa, K. Kudo, R. Jinnouchi, M. Osawa and Y. Morimoto, *ACS Catal.,* **8**(1), 694–700 (2018).
75. K. Kodama, T. Nagai, A. Kuwaki, R. Jinnouchi and Y. Morimoto, *Nature nanotechnology,* **16**(2), 140–147 (2021).
76. N. M. Markovic, H. A. Gasteiger and P. N. Ross Jr., *J. Phys. Chem.,* **99**(11), 3411–3415 (1995).
77. N. Markovic, H. A. Gasteiger and P. N. Ross, *J. Electrochem. Soc.,* **144**(5), 1591–1597 (1997).
78. A. Kongkanand and M. F. Mathias, *The journal of physical chemistry letters,* **7**(7), 1127–1137 (2016).
79. V. Yarlagadda, M. K. Carpenter, T. E. Moylan, R. S. Kukreja, R. Koestner, W. Gu, L. Thompson and A. Kongkanand, *ACS Energy Lett.,* **3**(3), 618–621 (2018).